Research Square

Preprints are preliminary reports that have not undergone peer review.
They should not be considered conclusive, used to inform clinical practice,
or referenced by the media as validated information.

A Dual-Responsive GA-Functionalized Mn-MSN Nanoplatform for Targeted Delivery of CD-2e and Enhanced Therapy of Hepatocellular Carcinoma

Yuqing Zheng
Liaoning University
Zhihang Li
Liaoning University
Yan Ma
Liaoning University
Hao Pan
Liaoning University
Lianrui Cao
Liaoning University
Yuqing Ni
Liaoning University
Cong Li
Liaoning University
Lijiang Chen
clj1172023@163.com
Liaoning University

Research Article

Keywords: Hepatocellular carcinoma, CD-2e, Mesoporous silica nanoparticles, Glycyrrhetinic acid, Dual responsive, Tumor microenvironment

Posted Date: August 3rd, 2026

DOI: https://doi.org/10.21203/rs.3.rs-10492081/v1

License: This work is licensed under a Creative Commons Attribution 4.0 International License.
Read Full License

Additional Declarations: No competing interests reported.

Abstract

Hepatocellular carcinoma (HCC) is characterized by high incidence and mortality rates, posing a severe challenge to global public health. CD-2e, a novel curcumol derivative, has demonstrated promising antitumor activity; however, its therapeutic development is hindered by poor aqueous solubility, limited circulation stability, weak cellular uptake, and low tumor accumulation efficiency. To overcome these limitations, we developed a CD-2e-loaded glycyrrhetinic acid (GA)-modified manganese-doped mesoporous silica nanoparticle system (GA-Mn-MSNs@CD-2e) for targeted and tumor microenvironment-responsive drug delivery. Mesoporous silica nanoparticles (MSNs) enhanced the loading capacity for CD-2e and helped improve its aqueous dispersibility, while GA modification promoted specific uptake by HCC cells through active targeting. After internalization, the tumor microenvironment triggered the cleavage of Mn-O bonds, enabling controlled release of CD-2e. Both *in vitro* and *in vivo* studies demonstrated that GA-Mn-MSNs@CD-2e significantly enhanced cellular uptake, prolonged tumor retention, and improved antitumor efficacy. In addition, GA-Mn-MSNs@CD-2e showed potential in modulating macrophage polarization and remodeling the tumor microenvironment. Overall, this intelligent nanodelivery system effectively addresses the major delivery barriers associated with CD-2e and provides a highly promising strategy for precise and efficient HCC therapy.

1. Introduction

According to data from the World Health Organization, more than 860,000 new cases of liver cancer and approximately 760,000 liver cancer-related deaths occurred worldwide in 2022, making it one of the malignant tumors that seriously threaten human health [1, 2]. Hepatocellular carcinoma (HCC) is the predominant pathological subtype of primary liver cancer, accounting for 75%-85% of cases [3–5]. Owing to its insidious onset, most patients with HCC are diagnosed at intermediate or advanced stages, when curative treatments such as surgical resection or liver transplantation are no longer feasible [6]. At present, local ablation, transcatheter arterial chemoembolization (TACE), radiotherapy, and systemic therapies mainly based on targeted agents and immunotherapeutic drugs represent important treatment options for patients who are not eligible for surgery [7–9]. However, systemic pharmacotherapy still faces several challenges, including insufficient drug accumulation at tumor sites, nonspecific biodistribution, limited therapeutic efficacy, and potential toxic side effects [10]. Therefore, the development of safe and efficient drug delivery systems with tumor-targeting capability is of great significance for improving the therapeutic outcomes of HCC [11–13].

Natural bioactive compounds have attracted considerable attention in anticancer drug development owing to their broad availability, favorable biosafety profiles, and potential for multi-pathway regulation [14]. As a representative example, curcumol has demonstrated significant inhibitory activity against various malignancies, including cervical cancer, rectal cancer, and lung cancer. Its antitumor mechanisms are highly diverse: curcumol can directly induce tumor cell death by interfering with key signaling pathways such as PI3K/Akt or by regulating the expression of pro-apoptotic proteins [15–17]. In addition, it can effectively remodel the tumor immune microenvironment by inducing macrophage

polarization from the tumor-promoting M2 phenotype toward the antitumor M1 phenotype [18, 19]. However, several inherent limitations, including poor aqueous solubility, weak target affinity, and low targeting specificity, have severely restricted its application barriers *in vivo*. To address these issues, a novel derivative, CD-2e, was successfully developed through rational structural modification by introducing hydrophilic amide groups and nitrogen-containing heterocycles at the C-8 position of curcumol [20]. This modification markedly increased the number of intramolecular hydrogen-bond acceptors (HBAs) and hydrogen-bond donors (HBDs), thereby not only improving the aqueous solubility and target-binding affinity of the parent compound but also substantially enhancing its antitumor activity. Previous studies have confirmed that CD-2e exerts potent antiproliferative effects against human hepatocellular carcinoma HepG2 cells by inducing cell-cycle arrest, promoting apoptosis, and modulating related signaling cascades [21]. Nevertheless, the translation of CD-2e for *in vivo* application still faces substantial drug delivery barriers. Its aqueous solubility remains insufficient to fully meet the requirements for efficient *in vivo* administration; free CD-2e is readily cleared from the bloodstream or inactivated through enzymatic metabolism; its transmembrane penetration is limited; and its retention time at tumor sites is short, making it difficult to maintain an effective local drug concentration. To overcome these *in vivo* delivery bottlenecks, the construction of intelligent nanocarrier-based delivery systems has emerged as a highly promising strategy for enhancing its antitumor efficacy [22].

The aberrant pathological features of the tumor microenvironment (TME) provide an important rationale for the design of intelligent delivery systems. Unlike normal tissues, tumor tissues typically exhibit a mildly acidic pH and elevated intracellular glutathione (GSH) levels [23, 24]. Mesoporous silica nanoparticles (MSNs) have been widely applied in tumor drug delivery owing to their stable inorganic framework, high specific surface area, and high drug-loading capacity [25]. In particular, the abundant silanol groups on their surface allow the facile introduction of functional groups, such as amino and thiol groups, through silane coupling reactions, thereby laying the foundation for the construction of targeted, stimuli-responsive, and multifunctional delivery platforms [26, 27]. On this basis, doping manganese (Mn) into the MSN framework can endow the nanocarrier with excellent TME-responsive properties. Mechanistically, Mn-O bonds remain relatively stable under normal physiological conditions but are highly susceptible to reduction and dissociation in the tumor-specific acidic and GSH-enriched microenvironment [28]. This specific stimuli-responsive mechanism not only effectively suppresses premature burst release of the drug in normal tissues, but also ensures precise, on-demand release of the payload within the tumor-targeted region [29, 30].

Glycyrrhetinic acid (GA), a clinically used hepatoprotective agent, possesses intrinsic antiproliferative activity against HCC and can bind with high affinity to receptors overexpressed on the surface of HCC cells [31, 32]. Based on this receptor-mediated specific interaction, GA is frequently employed as an ideal targeting ligand for surface modification of nanocarriers, thereby significantly enhancing the precise recognition and efficient uptake of delivery systems by HCC cells. In addition, GA can exert auxiliary immunomodulatory effects, promoting macrophage polarization toward an antitumor phenotype [33–35].

Based on the above rationale, to overcome the delivery barriers of the antitumor agent CD-2e, including poor aqueous solubility, limited circulation stability, and insufficient targeted accumulation, we constructed a GA-modified manganese-doped mesoporous silica intelligent nanoplatform (GA-Mn-MSNs@CD-2e) for the efficient loading and precise delivery of CD-2e (Scheme 1). In this intelligent delivery system, MSNs improve the aqueous dispersibility of CD-2e and protect it from premature clearance during systemic circulation. Meanwhile, surface-modified GA mediates active targeting, thereby enhancing the specific uptake of the nanocarrier by hepatocellular carcinoma cells. After cellular internalization, Mn-O bonds undergo cleavage in response to the tumor microenvironment, leading to disassembly of the nanostructural framework and responsive release of CD-2e. As a result, efficient tumor accumulation and precise on-demand drug release are successfully achieved. Both *in vitro* and *in vivo* studies demonstrated that GA-Mn-MSNs@CD-2e promoted drug uptake by hepatocellular carcinoma cells and significantly enhanced antitumor efficacy. In a subcutaneous H22 syngeneic hepatocellular carcinoma model, GA-Mn-MSNs@CD-2e prolonged drug accumulation at the tumor site and effectively inhibited tumor growth without inducing detectable organ or tissue toxicity. In addition, preliminary evidence indicated that this formulation possesses potential for modulating macrophage polarization and remodeling the tumor microenvironment. In summary, this intelligent delivery strategy effectively overcomes the clinical application limitations of CD-2e and provides a highly promising new approach for precise and efficient hepatocellular carcinoma therapy.

2. Materials and Methodology

2.1. Materials

The following materials were provided by the respective suppliers: Curcumol (Rongsheng Plant Co., Ltd., Ji'an, China); reduced glutathione, 1-phenylpiperazine, indocyanine green, cetyltrimethylammonium bromide, aminopropyltriethoxysilane, and dicyclohexylcarbodiimide (Macklin Biochemical Technology Co., Ltd., Shanghai, China); chloroacetyl chloride, triethylamine, tetraethyl orthosilicate, *N*,*N*-dimethylformamide, and dichloromethane, and methanol (Damao Chemical Reagent Factory, Tianjin, China); sodium hydride, $MnSO_4 \cdot H_2O$, GA, and *N*-hydroxy succinimide (Shanghai Aladdin Biochemical Tech Co., Ltd., Shanghai, China); tetrahydrofuran (Tianjin Fuyu Chemical Co., Ltd., Tianjin, China); ethyl acetate (Tianjin Yongda Chemical Reagent Co., Ltd., Tianjin, China); column chromatography silica gel (refined) (Qingdao Haiyang Chemical Co., Ltd., Qingdao, China); PBS, DMEM, fetal bovine serum, penicillin-streptomycin and 4% paraformaldehyde (Wuhan Servicebio Tech Co., Ltd., Wuhan, China); MTT reagent (Beijing Dingguo Changsheng Biotechnology Co., Ltd., Beijing, China); DMSO and AO-EB staining solution (Beijing Solarbio Science & Technology Co., Ltd., Beijing, China); rhodamine B dye and DAPI (Meilunbio Co., Ltd., Dalian, China). Anti-mouse F4/80-FITC, CD86-APC and CD206-PE (Thermo Fisher Scientific, MA, USA). ELISA kits (R&D Systems, Minneapolis, MN, USA).

2.2. Animals and cells

Specific pathogen-free KM mice (male, 18 ~ 22 g) were obtained from Liaoning Changsheng Biotech Co., Ltd. (Shenyang, China). Studies involving these animals were conducted following protocols approved by the Animal Care & Welfare Committee of Liaoning University, adhering to established ethical guidelines. Mice were housed under controlled conditions with the temperature maintained at 22 ± 2°C and a light/dark cycle of 12 hours. Mice had unrestricted access to food and water.

The H22 cell line was purchased from Wuhan Pricella Biotechnology Co., Ltd. The cells were cultured in DMEM medium supplemented with 10% fetal bovine serum (FBS) and 1% penicillin/streptomycin and maintained at 37°C in a humidified atmosphere containing 5% CO_2.

The HepG2 cell line was purchased from Shanghai Academy of Biological Sciences Cell Bank, Chinese Academy of Sciences. These cells were cultured in DMEM supplemented with 10% FBS and kept at 37°C in a humidified atmosphere containing 5% CO_2.

The murine macrophage RAW264.7 cell line was purchased from Guangzhou Jennio Biotech Co., Ltd. These cells were cultured in DMEM supplemented with 10% FBS and 1% penicillin/streptomycin solution and kept at 37°C in a humidified atmosphere containing 5% CO_2.

2.3. Establishment of a subcutaneous H22 hepatoma-bearing mouse model

A subcutaneous H22 hepatoma-bearing mouse model was established in KM mice by subcutaneous injection of an H22 ascites-derived cell suspension. Mice (for ascites culture) were injected intraperitoneally with 1×10^6 H22 cells. Following a 5- to 7-day incubation period, the mice were euthanized and the ascites (milky white or light yellow) were harvested. An equal volume of 0.9% saline was then added to the ascites to prepare a cell suspension. On day 0, 0.1 mL of this suspension was injected subcutaneously into the left axilla of mice to initiate pharmacodynamic studies [36, 37].

2.4. Synthesis of CD-2e

CD-2e was synthesized in two steps. Initially, 25 mmol of 1-phenylpiperazine was dissolved in anhydrous tetrahydrofuran (THF) and subsequently combined with 75 mmol of triethylamine (TEA). The mixture was then stirred at 25°C, and a THF solution containing 37.5 mmol of chloroacetyl chloride was added dropwise. Upon reaction completion, the mixture was collected and filtered, and the THF was evaporated. The resulting solution was extracted thrice, vacuum-pumped, and the organic solvents were removed from the filtrate, which was then dried to yield the intermediate product. In the second step, 7.5 mmol of sodium hydride was gradually introduced into a THF solution containing 5 mmol of curcumol, followed by refluxing at 70°C for 2 hours. After the reaction mixture was cooled, a THF solution of the intermediate product (6 mmol) was added. After the reaction, the solution was processed identically to the first step. The product was then purified via column chromatography. The structure of the products was characterized using ^{1}H-NMR (600-MHz, Bruker) in chloroform-d and Fourier transform infrared

spectroscopy (FT-IR, IRAffinity-1, Shimadzu) with a resolution of 2 cm^{-1}, conducting 64 scans ranging from 4000 to 500 cm^{-1}.

2.5. Preparation of GA-Mn-MSNs@CD-2e

2.5.1. Preparation of GA-Mn-MSNs

Employing a conventional sol-gel method, 225 mg of cetyltrimethylammonium bromide (CTAB) in ethanol was added dropwise to a NaOH solution (1.25 mmol/100 mL) under stirring, and the reaction system was heated to 80°C. After 30 minutes, 1 mL of tetraethyl orthosilicate (TEOS) and 0.5 mL of a $MnSO_4 \cdot H_2O$ solution (8 mg/mL) were gradually introduced into the mixture, which was then allowed to react for an additional 2 hours.

The mixture was left to settle overnight, after which the precipitate was collected and centrifuged at 5000 rpm for 10 minutes. The supernatant was discarded, and the lower layer was washed with purified water, followed by another centrifugation for 5 minutes. This layer was subsequently washed with anhydrous ethanol and centrifuged for a further 5 minutes. The sequence of centrifugation, washing, and centrifugation was repeated three times. The product was then dried under vacuum at 50°C and calcined at 550°C for 4 hours in a muffle furnace to yield Mn-incorporated mesoporous silica nanoparticles (Mn-MSNs). MSNs were synthesized using the same protocol as that used for Mn-MSNs, except that $MnSO_4 \cdot H_2O$ solution was not added [38].

To obtain the precursors (GA-NHS) for GA-Mn-MSNs, GA, Dicyclohexylcarbodiimide (DCC), and *N*-Hydroxy succinimide (NHS) were mixed in dichloromethane at a molar ratio of 1.2:1.2:1 and incubated at 30°C for 6 h. The precipitated dicyclohexylurea was removed by filtration, and the filtrate was concentrated under reduced pressure to obtain GA-NHS.

An appropriate amount of as-synthesized Mn-MSNs was weighed and completely dispersed in toluene. APTES was added under nitrogen protection, and the mixture was refluxed at 80°C for 9 h. The resulting product was filtered through organic membranes, and the filter residue was washed alternately with anhydrous ethanol and purified water, followed by drying to yield NH_2-Mn-MSNs.

A slight excess of GA-NHS was dispersed with NH_2-Mn-MSNs in a DMF solution containing TEA and refluxed at 80°C for 12 h. The product was then filtered through organic membranes, and the residue was washed alternately with anhydrous ethanol and purified water. After thorough drying, GA-Mn-MSNs were collected [39].

2.5.2. Loading of CD-2e

CD-2e was loaded into GA-Mn-MSNs using the solution impregnation method. A mixture of CD-2e and nanoparticles at a weight ratio of 1:3 was dissolved in methanol and stirred at 25°C for 12 hours. After loading, the precipitate was subjected to centrifugation, washed with methanol, and then dried to yield CD-2e-loaded nanoparticles.

2.6. Characterization of MSNs

The *zeta* potential, size, and particle size distribution of the MSNs were evaluated using a Zetasizer® (Nano-ZS90, Malvern). The morphological features of the MSNs were investigated using a scanning electron microscope (S-4800 SEM, Hitachi) and a transmission electron microscope (JEM-1200EX TEM, JEOL). For SEM analysis, MSNs dispersion was deposited onto dry silicon wafers, dried, gold-sputtered, and subsequently imaged under the microscope. For TEM, drops of MSNs dispersion were placed on a copper grid (200 mesh), dried, and then examined under the TEM.

For elemental composition and structure analysis, MSNs were prepared as samples for Energy Dispersive Spectrometer (EDS), X-Ray Diffraction (D8 ADVANCE XRD, Bruker), FTIR, and N_2 adsorption-desorption detection (ASAP 2460, Micromeritics).

To elucidate the loading pattern of CD-2e in GA-Mn-MSNs, GA-Mn-MSNs@CD-2e was subjected to differential scanning calorimetry (7000Series DSC, HITACHI) analysis.

2.7. *In vitro* release study

To assess the dual-sensitive drug release characteristics of CD-2e@GA-Mn-MSNs *in vitro*, this study employed PBS solutions with pH 7.4 to mimic the physiological environment, and a combination of pH 5.0 + 5 mM GSH to represent the acid and high GSH environment typically found in tumor cells. Each sample (3 mL) was sealed within a pre-conditioned dialysis membrane (MWCO, 3500 Da) and immersed in 30 mL of release medium containing 0.5% sodium dodecyl sulfate as a surfactant. The setup was protected from light and stirred at a constant rate of 180 rpm at 37 ± 0.5°C. At predetermined intervals (0.5, 1, 2, 4, 6, 8, 10, 12, 24, 36, 48, and 72 h), 1 mL of dialysate was extracted and immediately replenished with an equal volume of fresh release medium at the same temperature. The absorbance of CD-2e in the dialysate samples was measured spectrophotometrically at 246 nm, and the cumulative drug release efficiency (Er) was calculated using the following formula:

$$\mathrm{Er}\% = \frac{V_e \sum_1^{n-1} C_i + V_0 C_n}{M_{drug}}$$

V_e, displacement volume of the released medium; V_0, the total volume of release medium; C_i, the concentration of releasing fluid at *i* h of sampling; *n*, the number of releasing fluid replacements; M_{drug}, the mass of drug in MSNs.

2.8. Cytotoxicity of drugs against HepG2 *in vitro*

The cytotoxicity of CD-2e released from MSNs was evaluated using MTT assays *in vitro*. HepG2 cells were seeded into 96-well plates at a density of 1 × 10^4 cells/well, incubated, and allowed to stabilize for 24 h. 100 μL of various concentrations of the drug or MSNs were introduced and co-incubated with the cells for either 24 or 48 h. The cells were then treated with MTT solution (5 mg/mL) for 4 h, followed by

the addition of 150 μL/well of DMSO. The absorbance was measured using a microplate reader at 490 nm to assess cell viability.

2.9. HepG2 apoptosis analysis *in vitro*

HepG2 cells were resuspended in DMEM medium and seeded at a density of 1×10^6 cells/well into a 6-well plate. Following stabilization in an incubator at 37°C with 5% CO_2 for 24 h, the cells were exposed to CD-2e, Mn-MSNs@CD-2e, and GA-Mn-MSNs@CD-2e (each equivalent to 100 μM CD-2e) at 37°C for 4 h. Subsequently, the cells were washed with PBS and stained with an AO-EB solution for 10 minutes under light-proof conditions. Fluorescence images were captured using a fluorescence inverted microscope under blue light excitation.

2.10. *In vitro* repolarization of M2 TAMs

To evaluate the effect of GA-Mn-MSNs@CD-2e on macrophage polarization, RAW264.7 cells (2×10^5 cells/well) were seeded into 6-well plates. The cells were co-cultured with IL-4 (20 ng/mL) and H22 tumor supernatant for 12 h to establish an M2-polarized phenotype. Subsequently, the cells were treated with PBS, GA-Mn-MSNs, or GA-Mn-MSNs@CD-2e and incubated for an additional 48 h, during which IL-4 and tumor supernatant were maintained in the culture medium.

2.10.1. ELISA

ELISA was used to measure cytokine levels in cell culture supernatants. Cell culture supernatants were collected using ELISA to analyze IL-6 and TGF-β.

2.10.2. Flow cytometry

Cells were harvested and stained with anti-F4/80-FITC and anti-CD86-APC antibodies to identify M1-type RAW264.7 macrophages (F4/80 + CD86+). Concurrently, M2-type RAW264.7 macrophages (F4/80 + CD206+) were detected using anti-F4/80-FITC and anti-CD206-PE antibodies. Data acquisition and analysis were performed using a flow cytometer (FCM, Beckman Coulter, USA).

2.11. Uptake behavior of GA-Mn-MSNs@CD-2e by hepatocellular carcinomas cells

2.11.1. *In vitro* uptake behavior of HepG2

An appropriate quantity of RhB and Mn-MSNs (or GA-Mn-MSNs) was dissolved in pure water and subsequently stirred at 25°C for 12 h. The resultant precipitates were subjected to sequential washing with distilled water and anhydrous ethanol, followed by drying to yield Mn-MSNs@RhB and GA-Mn-MSNs@RhB.

To investigate the uptake behavior of different MSNs by HepG2 cells, HepG2 cells were first seeded in DMEM medium at a density of 2×10^5 cells/mL. RhB-labeled MSNs were then added, and the cells were

further incubated for 4 h. After incubation, the drug-containing medium was discarded, and the cells were gently washed twice with PBS to remove free particles that had not been internalized. DAPI was subsequently added, and the cells were stained for 10 min in the dark to label the nuclei. Finally, the intracellular distribution of RhB fluorescence was observed under a fluorescence inverted microscope (FIM).

To further quantitatively analyze the uptake efficiency of different nanoparticles by HepG2 cells, FCM was employed. Specifically, HepG2 cells were resuspended in DMEM medium, and the cell density was adjusted to 1×10^6 cells/mL. The cells were then aliquoted into sterile Eppendorf tubes and pre-incubated at 37°C for 1 h, followed by the addition of different RhB-labeled nanoparticles and further incubation for 4 h. In the competitive inhibition experiment, before the addition of GA-Mn-MSNs@RhB, the cells were pretreated with an excess of GA solution to competitively occupy the relevant binding sites on the cell membrane, thereby verifying the specificity of GA-mediated uptake. After incubation, the cells were collected by centrifugation, washed with PBS, fixed with 4% paraformaldehyde, and then subjected to FCM analysis.

2.11.2. *In vivo* targeting tumors studies

An appropriate amount of indocyanine green (ICG) and GA-Mn-MSNs was dissolved in anhydrous ethanol and stirred in an ice-cold water bath for 12 h. The precipitates were sequentially washed with purified water and dried to yield ICG-labeled GA-Mn-MSNs (GA-Mn-MSNs@ICG).

To evaluate the *in vivo* tumor-targeting capability of GA-Mn-MSNs, this study conducted fluorescence imaging using GA-Mn-MSNs@ICG. When the tumor volume reached a predetermined size, GA-Mn-MSNs@ICG was administered to mice via tail vein injection. Subsequently, fluorescence images were acquired at multiple time points (12, 24, 48, and 72 hours post-injection) using the AniView600 multimodal *in vivo* imaging system (Biolight Biotechnology Co., Ltd., Guangzhou, China).

At 72 hours post-injection, the mice were humanely euthanized, and fluorescence imaging of the major organs (heart, liver, spleen, lungs, kidneys and tumor) was performed using the same system. The distribution of ICG-labeled MSNs in the tissues was estimated by analyzing the regions of interest (ROI).

2.12. Anti-tumor efficacy of GA-Mn-MSNs@CD-2e *in vivo*

To evaluate the antitumor efficacy of GA-Mn-MSNs@CD-2e, a subcutaneous H22 syngeneic hepatocellular carcinoma model was established as described in Section 2.3. The mice were randomly divided into four groups (n = 10) and intravenously administered different formulations: 0.9% saline, free CD-2e, Mn-MSNs@CD-2e, and GA-Mn-MSNs@CD-2e (at a CD-2e-equivalent dose of 10 mg/kg). This dosing regimen was repeated every 5 days, and changes in body weight and tumor volume were recorded regularly. On day 10 after treatment initiation, four mice from each group were randomly selected and humanely euthanized. The tumors were excised, weighed, and photographed to evaluate the short-term tumor inhibitory effects of the different formulations. The tumor inhibition rate (TI) was calculated according to the following equation:

$TI = (m_{saline} - m_{treat}) / m_{control} \times 100\%$

m_{saline}, the tumor mass in the saline group, and m_{treat}, the tumor mass in the different treatment groups.

The collected tumor tissues were subsequently subjected to H&E staining, and histopathological changes were observed under a digital microscope. The remaining mice were further monitored for changes in body weight and survival time to comprehensively evaluate the i*n vivo* therapeutic efficacy and safety of the different formulations.

2.13. Detection of tumor-associated inflammatory factors

To evaluate the potential regulatory effect of GA-Mn-MSNs@CD-2e on the tumor immune microenvironment, a separate cohort of H22 tumor-bearing mice was established for the detection of tumor-associated inflammatory factors. When the tumor volume reached the predetermined threshold, the mice were randomly divided into four groups (n = 6): saline, CD-2e, GA-Mn-MSNs, and GA-Mn-MSNs@CD-2e.

On day 10 after treatment initiation, mice in each group were humanely euthanized, and tumor tissues were collected. The excised tumor tissues were washed with pre-chilled PBS, weighed, and homogenized in an ice bath. The tissue homogenates were then centrifuged at 4°C, and the supernatants were collected. The levels of immune-related mediators, including TGF-β, PGE2, IL-6, iNOS, IL-10, Arg-1 and CSF-1 in the tumor tissue homogenate supernatants were measured using commercial ELISA kits according to the manufacturers' instructions.

2.14. Biosafety evaluation

To further evaluate the *in vivo* safety of GA-Mn-MSNs@CD-2e, the major organs of mice, including the heart, liver, spleen, lungs, and kidneys, were collected after completion of the treatment. The excised organs were rinsed with PBS, immediately fixed in 4% paraformaldehyde, and then subjected to paraffin embedding, sectioning, and H&E staining. Histomorphological changes were subsequently examined under a digital microscope.

Meanwhile, blood samples were collected from the mice for serum biochemical analysis. Blood was drawn into anticoagulant-free collection tubes and allowed to stand at room temperature for 1 h, followed by centrifugation to separate the serum. Serum levels of lactate dehydrogenase (LDH), creatine kinase-MB (CK-MB), aspartate aminotransferase (AST), alanine aminotransferase (ALT), blood urea nitrogen (BUN), and creatinine (CREA) were measured using commercial assay kits (Merck KGaA, Darmstadt, Germany) according to the manufacturer's instructions, in order to assess cardiac, hepatic, and renal function, respectively.

2.15. Statistical analysis

All data are expressed as means ± standard deviation, and comparisons among groups were assessed using two-tailed Student's t-tests and one-way ANOVA. All data were statistically analyzed using

GraphPad Prism version 8.0.2 (GraphPad Software Inc., USA). A *P*-value of less than 0.05 was considered statistically significant for all tests.

3. Results

3.1. Characterization of CD-2e

The synthetic route of CD-2e was depicted in Fig. 1A, with the resulting product manifesting as a loose, white, crystalline powder. As evidenced in Fig. 1B, the ^{1}H NMR spectra of the synthesized compound exhibited 38 distinct hydrogen peaks, aligning with the predictions provided by the ChemDraw software. ^{1}H NMR (600 MHz, chloroform*d*) δ 7.31–7.24 (m, 3H), 6.96–6.87 (m, 2H), 4.87 (t, *J* = 2.1 Hz, 2H), 4.41 (d, *J* = 12.2 Hz, 1H), 4.24 (d, *J* = 12.2 Hz, 1H), 3.91–3.83 (m, 2H), 3.79 (dt, *J* = 18.7, 6.9 Hz, 2H), 3.74 (q, *J* = 8.8, 6.8 Hz, 1H), 3.18 (q, *J* = 7.7, 6.5 Hz, 4H), 2.56 (d, *J* = 14.9 Hz, 1H), 2.49 (d, *J* = 14.7 Hz, 1H), 2.18 (t, *J* = 10.1 Hz, 1H), 2.08 (t, *J* = 12.4 Hz, 1H), 1.95 (tt, *J* = 15.0, 8.1 Hz, 1H), 1.87 (p, *J* = 7.8 Hz, 1H), 1.79 (td, *J* = 11.8, 6.6 Hz, 1H), 1.73–1.62 (m, 3H), 1.48–1.39 (m, 1H), 1.18 (dd, *J* = 12.6, 6.5 Hz, 1H), 1.00–0.93 (m, 6H), 0.86 (d, *J* = 6.4 Hz, 3H). ESIMS (m/z): 461.2$[M + Na]^{+}$, 477.2$[M + K]^{+}$.

For FT-IR, appropriate amounts of curcumol or CD-2e were combined with KBr powder and co-milled to produce thin flakes. As illustrated in Fig. 1C, the FT-IR spectra revealed that the peak at 3420 cm^{-1}, present in curcumol, was absent in CD-2e. Additionally, the spectra displayed stretching vibrations at 1690 – 1650 cm^{-1}, 1600 – 1590 cm^{-1}, and 1250 – 1210 cm^{-1}, which correspond to the amide group (-CONR), benzene ring (C = C), and amine (C-N) stretching vibrations, respectively. The characterization of the CD-2e structure was thus confirmed through the ^{1}H-NMR and FT-IR results.

3.2. Characterization of MSNs

3.2.1. Morphological characterization of MSNs

The preparation procedure of GA-Mn-MSNs@CD-2e is illustrated in Fig. 2A [40]. First, CTAB was used as a structure-directing agent, and Mn-doped mesoporous silica nanoparticles (Mn-MSNs) were synthesized via a co-condensation method. The particle surface was then aminated with APTES to obtain NH_2-Mn-MSNs. Subsequently, GA, activated by DCC/NHS, was conjugated to the surface amino groups to yield GA-Mn-MSNs. Finally, CD-2e was loaded to construct the GA-Mn-MSNs@CD-2e nano-drug delivery system. Because GA can specifically bind to overexpressed receptors on the surface of hepatocellular carcinoma cells, this modification strategy can enhance the uptake of the nanoplatform by liver cancer cells, while further addressing the poor aqueous solubility and low bioavailability of CD-2e.

As shown in Fig. 2B, MSNs appeared as a white, loose powder. After Mn doping, the resulting Mn-MSNs exhibited a light brown color. Following further GA modification, GA-Mn-MSNs appeared brownish-yellow, indicating that changes in the surface composition of the materials could lead to pronounced alterations

in their macroscopic appearance. DLS results (Fig. 2C) showed that the average hydrodynamic diameters of Mn-MSNs and GA-Mn-MSNs were 380.2 ± 6.7 nm and 266.4 ± 11.2 nm, respectively, with PDIs of 0.225 ± 0.030 and 0.331 ± 0.025, suggesting that GA modification induced certain changes in both particle size and dispersibility. Further zeta potential analysis (Fig. 2D) revealed that the surface potentials of MSNs, Mn-MSNs, NH_2-Mn-MSNs, and GA-Mn-MSNs were − 29.2 ± 0.9 mV, − 19.5 ± 0.7 mV, + 11.6 ± 1.0 mV, and − 25.8 ± 1.9 mV, respectively. Notably, after amination, the particle surface charge shifted from negative to positive, whereas after GA conjugation it reverted to a negative value, confirming the successful amino functionalization and subsequent GA grafting. TEM (Figs. 2E-F) and SEM (Fig. 3A) further demonstrated that the prepared nanoparticles were generally spherical, relatively uniform in dispersion, and retained a well-defined mesoporous architecture and characteristic rough surface morphology. Collectively, these characterization results indicate that GA-modified Mn^{2+}-incorporated MSNs were successfully constructed.

3.2.2. Structural characterization of MSNs

As shown in Fig. 3B, the EDS spectrum of Mn-MSNs displayed characteristic peaks of O, Si, and Mn, indicating the successful incorporation of Mn into the sample. Combined with the elemental quantitative analysis results in Table 1, the mass percentage and atomic percentage of Mn were 0.75% and 0.26%, respectively, further confirming that Mn^{2+} was successfully doped into the MSN system [41, 42].

Table 1
Element table of MnMSNs.

Element	Percentage of Weight	Percentage of Atom
O	65.08	76.78
Si	34.17	22.97
Mn	0.75	0.26
Total	100.00	-

The XRD patterns (Fig. 3C) showed that the diffraction profiles of MSNs and Mn-MSNs were essentially identical. Both samples exhibited a prominent broad peak at around 2θ = 22.5°, which is a typical characteristic peak of amorphous silica. These results indicate that the original amorphous silica framework of the MSNs was preserved during Mn^{2+} doping, suggesting that the introduction of Mn^{2+} did not disrupt the fundamental structural features of the mesoporous silica material. As shown in Fig. 3D, the FT-IR spectra of Mn-MSNs, NH_2-Mn-MSNs, and GA-Mn-MSNs all displayed the characteristic absorption bands of mesoporous silica materials, including the symmetric stretching vibration of Si-O-Si at 799 cm^{-1} and the asymmetric stretching vibration of Si-O-Si at 1087 cm^{-1}. These characteristic bands indicate that all samples retained an intact siloxane framework. Notably, GA-Mn-MSNs exhibited aliphatic C-H absorption bands in the region of 2920 − 2850 cm^{-1}, and these features were consistent

with the spectrum of GA, indicating that GA had been successfully conjugated onto the nanoparticle surface.

As shown in Fig. 3E, the N_2 adsorption-desorption isotherms of both Mn-MSNs and GA-Mn-MSNs exhibited the typical characteristics of type IV mesoporous materials, accompanied by a distinct hysteresis loop, indicating that both materials retained a relatively well-preserved mesoporous structure [43]. Further examination of the pore size distribution curves in Fig. 3F showed that the pore diameters of both samples were mainly concentrated around 2 nm, suggesting a relatively narrow pore size distribution and comparatively regular pore channel structure. BET analysis demonstrated that, compared with Mn-MSNs, GA-Mn-MSNs showed decreases in both specific surface area and pore volume. This may be attributed to partial coverage of the particle surface by GA molecules after modification, or the occupation of part of the pore space, thereby reducing the accessible surface area and effective pore volume available to N_2 molecules. Nevertheless, GA-Mn-MSNs still maintained the characteristic adsorption behavior of mesoporous materials, indicating that GA modification did not compromise the original mesoporous framework of the material. The specific surface area, pore volume, and pore size of Mn-MSNs and GA-Mn-MSNs are listed in Table 2.

Table 2
Specific surface area, average pore size, and pore volume of Mn-MSNs and GAMnMSNs.

Preparation	Mn-MSNs	GA-Mn-MSNs
BET Surface Area	1088.3 ± 24.6 m^2/g	572.3 ± 13.8 m^2/g
Pore Volume	0.705 ± 0.021 cm^3/g	0.537 ± 0.016 cm^3/g
Pore Diameter	2.1 ± 0.1 nm	2.0 ± 0.1 nm

To investigate the physical state of CD-2e in the carrier, DSC analysis was performed on CD-2e, GA-Mn-MSNs, GA-Mn-MSNs@CD-2e, and the physical mixture of GA-Mn-MSNs + CD-2e. As shown in Fig. 3G, GA-Mn-MSNs exhibited no obvious endothermic or exothermic peaks within the temperature range of 30 ~ 350°C. In contrast, the physical mixture still showed the characteristic endothermic peak of CD-2e at around 90 ~ 100°C, indicating that simple physical mixing did not alter the original thermal properties of CD-2e. However, in the DSC curve of GA-Mn-MSNs@CD-2e, this characteristic peak was markedly weakened or even disappeared, and the overall curve profile was more similar to that of GA-Mn-MSNs. These results suggest that CD-2e no longer existed in its original crystalline state within the carrier, but was successfully loaded into GA-Mn-MSNs in an amorphous form [44].

3.3. *In vitro* release profiles of MSNs

As shown in Fig. 3H, the cumulative *in vitro* release behavior of CD-2e under simulated tumor microenvironment conditions was evaluated using the dialysis method. Under pH 7.4 conditions, both GA-Mn-MSNs@CD-2e and Mn-MSNs@CD-2e exhibited relatively low drug release, with cumulative

release rates of only 17.51% and 20.11%, respectively, within 72 h, indicating that both mesoporous carriers possessed good drug-retention capability under physiological conditions. GA modification could further retard the release of CD-2e to a certain extent. By contrast, pH 5.0 + 5 mM GSH conditions, the cumulative release of GA-Mn-MSNs@CD-2e increased markedly, reaching 35.53% and 53.87% at 72 h, respectively. These results demonstrate that GA-Mn-MSNs@CD-2e possesses distinct dual pH/GSH-responsive release behavior: drug release is relatively slow in a neutral physiological environment, which helps minimize premature leakage, whereas release is significantly accelerated in the acid and highly reductive simulated tumor microenvironment, thereby favoring enhanced drug release efficiency at the tumor site [45, 46].

3.4. MTT assay

The effects of the unloaded carriers on HepG2 cells were evaluated by co-incubating HepG2 cells with Mn-MSNs or GA-Mn-MSNs for 24 h, followed by measurement of cell viability using a microplate reader. As shown in Fig. 4A, after treatment with Mn-MSNs, cell viability was generally maintained within the range of 80% ~ 100%, and remained above 80% even at relatively high concentrations, indicating that Mn-MSNs possessed good cytocompatibility. In contrast, the GA-Mn-MSNs-treated group showed a marked reduction in cell viability, to approximately 55% ~ 65%, suggesting that GA modification endowed the carrier with a certain degree of intrinsic antitumor activity. Notably, cell viability in the GA-Mn-MSNs group did not decrease further significantly with increasing concentration, which confirms the biosafety of GA-Mn-MSNs.

HepG2 cells were further co-incubated with free CD-2e, Mn-MSNs@CD-2e, and GA-Mn-MSNs@CD-2e for 24 h and 48 h, respectively, to evaluate the cytotoxicity of the different drug-loaded systems (Fig. 4B). At 24 h, the overall cell viability followed the order of CD-2e > Mn-MSNs@CD-2e > GA-Mn-MSNs@CD-2e, indicating that loading CD-2e into Mn-MSNs and GA-Mn-MSNs significantly enhanced its inhibitory effect on HepG2 cells. Compared with the free CD-2e and Mn-MSNs@CD-2e groups, the GA-Mn-MSNs@CD-2e group showed weaker concentration dependence and exhibited a plateau trend at medium to high concentrations, which may be related to the limited number of GA receptors on the surface of HepG2 cells and the saturation of receptor-mediated uptake. After 48 h, the inhibitory effect of the Mn-MSNs@CD-2e group on HepG2 cells was further enhanced compared with that at 24 h, suggesting that Mn-MSNs facilitated sustained drug release. In contrast, the GA-Mn-MSNs@CD-2e group maintained strong inhibitory activity at both 24 h and 48 h, indicating that it had already achieved high cytotoxic efficiency at an earlier stage. The IC_{50} values presented in Table 3 further confirmed these findings, with the GA-Mn-MSNs@CD-2e group showing the lowest IC_{50} values at both 24 h and 48 h, demonstrating the most potent antitumor activity [47].

Table 3
IC_{50} Values of HepG2 Cells with Different Formulations.

24 h	CD-2e	Mn-MSNs@CD-2e	GA-Mn-MSNs@CD-2e
	131.90 ± 14.14	**15.04 ± 4.83**	**1.87 ± 0.91**
48 h	104.30 ± 9.59	13.43 ± 3.51	1.30 ± 0.54

3.5. Apoptosis analysis

Apoptosis in HepG2 cells after treatment with free CD-2e, Mn-MSNs@CD-2e, and GA-Mn-MSNs@CD-2e was evaluated using AO-EB staining, and the results are shown in Fig. 4C. In the free CD-2e group, most cells exhibited green fluorescence and largely retained intact morphology, with only slight morphological changes observed in a small number of cells. In contrast, in the Mn-MSNs@CD-2e group, the number of morphologically abnormal cells increased. Some cells displayed apoptotic features, such as shrinkage, aggregation, and chromatin condensation, and occasional yellow-green/orange fluorescent signals were observed, suggesting the occurrence of apoptosis. After treatment with GA-Mn-MSNs@CD-2e, the total number of cells was reduced, and the proportion of morphologically abnormal cells increased further. Relatively more yellow-green/orange fluorescent cells were observed compared with the other groups, indicating that this formulation induced more pronounced apoptosis in HepG2 cells. These findings are consistent with the cell viability results, demonstrating that GA-Mn-MSNs@CD-2e can more effectively inhibit HepG2 cell survival and promote apoptosis.

3.6. Promoting TAMs Repolarization toward the M1 Phenotype

Repolarizing tumor-promoting M2 macrophages into the antitumor M1 phenotype can effectively alleviate the immunosuppressive microenvironment, thereby synergistically enhancing overall antitumor therapeutic efficacy [48]. In this study, an M2-like macrophage model was successfully established *in vitro* using IL-4 and tumor-conditioned supernatant [49], followed by treatment with different formulations for 48 h to evaluate their effects on macrophage repolarization (Fig. 4D). The expression levels of M1/M2 polarization-related cytokines in the cell culture supernatants were further determined by ELISA, while the expression of the M1 surface marker CD86 and the M2 surface marker CD206 was analyzed by flow cytometry. Consistent results from ELISA and flow cytometry showed that cells in the control group exhibited a typical M2-like immunosuppressive phenotype. In contrast, treatment with GA-Mn-MSNs@CD-2e increased the secretion of the pro-inflammatory cytokine IL-6 and markedly elevated the proportion of CD86-positive cells (Fig. 4E-F and S1). This pronounced repolarization effect can be mainly attributed to the intrinsic immunomodulatory activity of the loaded drug CD-2e, which effectively suppresses M2-associated immunosuppressive signaling and promotes the expression of M1-related pro-inflammatory factors. Meanwhile, GA modification on the carrier surface may further enhance CD-2e-mediated polarization regulation through its own immunomodulatory properties. These results indicate that GA-Mn-MSNs@CD-2e exhibits promising potential in driving TAM repolarization toward the antitumor M1 phenotype and remodeling the tumor immune microenvironment.

3.7. *In vitro* uptake behavior of HepG2 cells

To evaluate the cellular uptake capacities of different nanosystems in HepG2 cells, Mn-MSNs and GA-Mn-MSNs were labeled with RhB as a fluorescent probe and analyzed by FIM and FCM [50]. Previous studies have shown that GA can specifically bind to overexpressed receptors on the surface of hepatocellular carcinoma cells; therefore, GA modification was expected to promote the targeted endocytosis of nanoparticles. As shown in Fig. 5A, the free RhB group exhibited only weak intracellular red fluorescence, whereas the Mn-MSNs@RhB group showed an enhanced fluorescence signal, indicating that the nanocarrier could effectively increase probe accumulation in HepG2 cells. Furthermore, the GA-Mn-MSNs@RhB group displayed the strongest red fluorescence signal, demonstrating that GA modification significantly enhanced the uptake of nanoparticles by HepG2 cells.

The FCM results (Fig. 5B) further confirmed these findings. Compared with the Mn-MSNs@RhB group, the mean fluorescence intensity of the GA-Mn-MSNs@RhB group increased significantly. After pretreatment with excess free GA, the fluorescence intensity of the GA-Mn-MSNs@RhB group decreased markedly, indicating that GA-related binding sites on the cell membrane were competitively occupied, thereby weakening the receptor-mediated uptake of GA-modified nanoparticles. Taken together, the efficient internalization of GA-Mn-MSNs in HepG2 cells was not simply attributable to the nanoparticles themselves, but was mainly closely associated with GA-mediated specific recognition.

3.8. *In vivo* tumor targeting ability

To investigate the effective accumulation of GA-Mn-MSNs in the tumor region, we utilized ICG as a fluorescent probe to label MSNs and performed both *in vivo* and *ex vivo* fluorescence imaging of tumor-bearing mice at specified time points (Fig. 5C-D). Following injection, the fluorescence intensity at the tumor site in both groups exhibited dynamic changes over time [51]. Quantitative ROI analysis revealed that the average radiant efficiency at the tumor site in the GA-Mn-MSNs@ICG group was significantly higher than that in the non-targeted Mn-MSNs@ICG group at all time points post-injection. Furthermore, GA-Mn-MSNs@ICG demonstrated stronger initial accumulation and a more sustained fluorescent signal in the tumor region, maintaining a high fluorescence intensity even 72 hours after administration.

Ex vivo imaging of major organs and tumor tissues was conducted 72 hours post-injection (Fig. 5E). The results showed that both materials exhibited high distribution in the liver, which aligns with the typical metabolic pattern of nanoparticles via the reticuloendothelial system (RES). However, quantitative analysis indicated that the accumulation of GA-Mn-MSNs@ICG in tumor tissues was significantly greater than that of Mn-MSNs@ICG. Collectively, these results demonstrate that the surface modification with GA significantly enhances the tumor-targeting capability of Mn-MSNs and prolongs their retention time within tumor tissue. This favorable targeting behavior is primarily attributed to the GA-mediated active targeting effect.

3.9. *In vivo* therapeutic effects of HCC by GA-Mn-MSNs@CD-2e

To verify the *in vivo* antitumor efficacy of GA-Mn-MSNs@CD-2e, a murine hepatocellular carcinoma model was established by inoculation with H22 cells. When the tumor volume reached the predetermined threshold (defined as Day 0), the mice were randomly assigned to four groups (Saline, CD-2e, Mn-MSNs@CD-2e, and GA-Mn-MSNs@CD-2e) and received the corresponding treatments. The results showed (Fig. 6A) that, compared with the Saline group and the free CD-2e group, tumor growth was markedly inhibited in both the Mn-MSNs@CD-2e group and the GA-Mn-MSNs@CD-2e group, with the GA-Mn-MSNs@CD-2e group exhibiting the most pronounced antitumor effect. *Ex vivo* tumor images (Fig. 6B) and the tumor inhibition rate analysis (Fig. 6C) further confirmed that the GA-Mn-MSNs@CD-2e group achieved the highest tumor inhibition rate, reaching 62.23%, suggesting that GA modification can further enhance the *in vivo* therapeutic efficacy of this nanodelivery system.

Changes in body weight can, to a certain extent, reflect overall tolerability during treatment. As shown in Fig. 6D, body weight decreased to varying degrees in all groups during the early stage of the experiment; however, it tended to stabilize in the GA-Mn-MSNs@CD-2e group during the later treatment period, suggesting that this delivery system has favorable *in vivo* tolerability. Meanwhile, survival analysis (Fig. 6E) showed that the survival rates of mice in both the Saline and CD-2e groups declined to 0 by Day 40, whereas the survival rate in the GA-Mn-MSNs@CD-2e group remained at 87.5%, which was markedly higher than that in the Mn-MSNs@CD-2e group (37.5%). These findings further indicate that GA-Mn-MSNs@CD-2e exhibits superior *in vivo* therapeutic efficacy. The H&E staining results of tumor tissues (Fig. 6F) further supported the above conclusions. Compared with the saline group, more pronounced cellular damage and necrosis were observed in the tumor tissues of the GA-Mn-MSNs@CD-2e group, suggesting that it can inhibit tumor progression more effectively.

In the hepatocellular carcinoma microenvironment, the polarization status of TAMs is a critical determinant of immunosuppression and tumor progression. Therefore, ELISA was performed to quantify the levels of macrophage polarization-related immunomodulatory factors in tumor tissues from different treatment groups. As shown in Fig. 6G and S2, the GA-Mn-MSNs@CD-2e delivery system significantly downregulated the expression of M2 phenotype-associated immunosuppressive factors, including TGF-β1, PGE2, and IL-10, in tumor tissues. Meanwhile, it upregulated the levels of M1 phenotype-associated pro-inflammatory mediators, such as IL-6 and iNOS. This effect can be primarily attributed to the ability of CD-2e to induce macrophage polarization toward the antitumor M1 phenotype, together with the synergistic immunomodulatory activity exerted by GA on the nanocarrier surface. Collectively, these findings suggest that GA-Mn-MSNs@CD-2e not only directly kills tumor cells, but also possesses potential for reversing TAM polarization imbalance and remodeling the tumor immune microenvironment, thereby synergistically enhancing the overall antitumor efficacy (**Fig. S3**).

3.10. Biosafety evaluation

Good biosafety is an important indicator for evaluating the application potential of drug formulations [46, 52]. At the end of treatment, the heart, liver, spleen, lung, and kidney were collected from mice in the Healthy, CD-2e, Mn-MSNs@CD-2e, and GA-Mn-MSNs@CD-2e groups for H&E staining. As shown in Fig. 7A, no obvious pathological damage was observed in sections of the major organs from any group. Cellular morphology and tissue architecture remained largely normal, suggesting that these treatments did not cause significant toxic effects on the vital organs of the mice. Notably, no evident histological abnormalities were observed in the major organs of the GA-Mn-MSNs@CD-2e group, indicating that this formulation possesses favorable *in vivo* biosafety. In addition, as shown in **Fig. S4**, compared with the healthy groups, no significant differences (ns) were detected in serum levels of LDH, CK-MB, AST, ALT, BUN, or CREA among the treatment groups, and no obvious abnormal fluctuations were observed. These results further suggest that GA-Mn-MSNs@CD-2e did not induce evident cardiotoxicity, hepatotoxicity, or nephrotoxicity *in vivo*, and therefore exhibits good biosafety.

4. Conclusion

In this study, we successfully developed an intelligent mesoporous silica nanoparticle platform with GA surface modification and Mn incorporation into the framework (GA-Mn-MSNs@CD-2e), aiming to achieve precise targeting and effective therapy for HCC. This nanosystem effectively overcomes the major *in vivo* delivery barriers of the novel curcumol derivative CD-2e, including poor aqueous solubility, limited targeting capability, and rapid systemic clearance. By exploiting GA receptor-mediated active targeting, the nanosystem enables efficient uptake and prolonged retention of drug-loaded nanoparticles at HCC lesions. In addition, it can specifically respond to the mildly GSH conditions of the TME. Under these stimuli, cleavage of Mn-O bonds triggers disassembly of the nanostructural framework, thereby enabling precise, on-demand release of CD-2e. Importantly, beyond exerting direct antitumor effects, this delivery platform can also drive the polarization of TAMs toward an antitumor phenotype, indicating its potential to remodel the tumor immune microenvironment. Both *in vitro* and *in vivo* studies consistently confirmed that GA-Mn-MSNs@CD-2e significantly inhibits tumor growth without inducing evident tissue toxicity. In summary, this multifunctional intelligent delivery strategy not only addresses key bottlenecks limiting the clinical translation of CD-2e, but also provides a highly promising new approach for safe, precise, and efficient synergistic therapy of HCC.

Declarations

Ethical approval

Not applicable.

Competing interests

The authors declare no competing interests.

Funding

This research work was supported by the Department of Science and Technology of Liaoning Province of China (2024JH2/102500018), the Department of Education of Liaoning Province of China (LJ212410140022), the Youth Project of Liaoning Provincial Department of Education (JYTQN2023188), the Doctoral Start-up Project of Liaoning Provincial Department of Science and Technology (2023-BS086), the Basic Scientific Research Project of Liaoning University for Graduate Students (LNUYJS017), the Basic Scientific Research Project of Liaoning University, and the Youth Scientific Research Fund Project of Liaoning University.

Author Contribution

Z.Y.Q.: Writing – review & editing, Project administration. L.Z.H.: Writing – original draft, Methodology, Investigation. M.Y.: Methodology, Investigation. P.H.: Methodology, Investigation. C.L.R.: Methodology, Investigation. N.Y.Q.: Methodology, Investigation. L.C.: Funding acquisition. C.L.J.: Supervision, Resources, Funding acquisition.

Data Availability

No datasets were generated or analyzed during the current study.

References

1. Bray, F., Laversanne, M., Sung, H., Ferlay, J., Siegel, R. L., Soerjomataram, I., & Jemal, A. (2024). Global cancer statistics 2022: GLOBOCAN estimates of incidence and mortality worldwide for 36 cancers in 185 countries. *C Ca: A Cancer Journal For Clinicians*, *74*(3), 229–263. https://doi.org/10.3322/caac.21834
2. Zhou, J., Sun, H., Wang, Z., Cong, W., et al. (2023). Guidelines for the Diagnosis and Treatment of Primary Liver Cancer (2022 Edition). *Liver Cancer*, *12*(5), 405–444. https://doi.org/10.1159/000530495
3. Singal, A. G., Lampertico, P., & Nahon, P. (2020). Epidemiology and surveillance for hepatocellular carcinoma: New trends. *Journal Of Hepatology*, *72*(2), 250–261. https://doi.org/10.1016/j.jhep.2019.08.025
4. Pu, J., Zhao, Y., Zhang, S., Wu, T., Liu, R., Yuan, T., He, S., Hao, Q., & Zhu, H. (2025). Mapping the knowledge domains of literature on hepatocellular carcinoma and liver failure: a bibliometric approach. *Frontiers In Oncology*, *15*, 1529297. https://doi.org/10.3389/fonc.2025.1529297
5. Chidambaranathan-Reghupaty, S., Fisher, P. B., & Sarkar, D. (2021). Chapter One - Hepatocellular carcinoma (HCC): Epidemiology, etiology and molecular classification, in: D. Sarkar, P.B. Fisher (Eds.), Adv. Cancer Res., Academic Press pp. 1–61. https://doi.org/10.1016/bs.acr.2020.10.001

6. Qiu, J., Huang, Z., He, W., Wang, C., Xie, C., Shen, J., Cai, M., Yuan, Y., Zou, R., Li, B., & Yuan, Y. (2026). Sintilimab and lenvatinib plus hepatic arterial infusion chemotherapy and embolization as conversion therapy for uHCC: A phase 2 trial. *Med*, *7*(6), 101132. https://doi.org/10.1016/j.medj.2026.101132
7. Xie, D. Y., Zhu, K., Ren, Z. G., Zhou, J., Fan, J., & Gao, Q. (2023). A review of 2022 Chinese clinical guidelines on the management of hepatocellular carcinoma: updates and insights. *Hepatobiliary Surg Nutr*, *12*(2), 216–228. https://hbsn.amegroups.org/article/view/110837
8. Mak, L. Y., Wong, D. K. H., Pollicino, T., Raimondo, G., Hollinger, F. B., & Yuen, M. F. (2020). Occult hepatitis B infection and hepatocellular carcinoma: Epidemiology, virology, hepatocarcinogenesis and clinical significance. *Journal Of Hepatology*, *73*(4), 952–964. https://doi.org/10.1016/j.jhep.2020.05.042
9. Wang, C. I., Chu, P. M., Chen, Y. L., Lin, Y. H., & Chen, C. Y. (2021). Chemotherapeutic Drug-Regulated Cytokines Might Influence Therapeutic Efficacy in HCC. *International Journal Of Molecular Sciences*, *22*(24). https://doi.org/10.3390/ijms222413627
10. Gomerdinger, V. F., Nabar, N., & Hammond, P. T. (2025). Advancing engineering design strategies for targeted cancer nanomedicine. *Nature Reviews Cancer*, *25*(9), 657–683. https://doi.org/10.1038/s41568-025-00847-2
11. Yu, X., Zhang, Q., Wang, L., Zhang, Y., & Zhu, L. (2025). Engineered nanoparticles for imaging and targeted drug delivery in hepatocellular carcinoma. *Exp Hematol Oncol*, *14*(1), 62. https://doi.org/10.1186/s40164-025-00658-z
12. Tian, T., Ruan, J., Zhang, J., Zhao, C. X., Chen, D., & Shan, J. (2022). Nanocarrier-Based Tumor-Targeting Drug Delivery Systems for Hepatocellular Carcinoma Treatments: Enhanced Therapeutic Efficacy and Reduced Drug Toxicity. *Journal Of Biomedical Nanotechnology*, *18*(3), 660–676. https://doi.org/10.1166/jbn.2022.3297
13. Cosma, M., Mocan, T., Delcea, C., Pop, T., Mosteanu, O., & Mocan, L. (2025). Gold Nanoparticles as Targeted Drug Delivery Systems for Liver Cancer: A Systematic Review of Tumor Targeting Efficiency and Toxicity Profiles. *International Journal Of Molecular Sciences*, *26*(16). https://doi.org/10.3390/ijms26167917
14. Li, D., Wang, J., Tuo, Z., Yoo, K. H., Yu, Q., Miyamoto, A., Zhang, C., Ye, X., Wei, W., Wu, R., & Feng, D. (2024). Natural products and derivatives in renal, urothelial and testicular cancers: Targeting signaling pathways and therapeutic potential. *Phytomedicine*, *127*, 155503. https://doi.org/10.1016/j.phymed.2024.155503
15. Xie, J., Zhu, Y., Bai, H., Song, Z., Qiu, S., Xie, Y., & Wan, S. (2025). Multi-omics analysis of the anti-cancer effects of curcumol in endometrial carcinoma. *Frontiers In Pharmacology*, *16*, 1565959. https://doi.org/10.3389/fphar.2025.1565959
16. Zhao, W., Yan, Q., Liu, L., Hou, D., Xiang, D., Tang, D., Li, L., Shen, W., Tao, W., Cheng, H., & Sun, D. (2025). Curcumol promotes ferroptosis of colon cancer by targeting the ubiquitination and

degradation of GPX4. *J Tradit Complement Med*, *15*(2), 170–181. https://doi.org/10.1016/j.jtcme.2024.08.006

17. Wei, W., Rasul, A., Sadiqa, A., Sarfraz, I., Hussain, G., Nageen, B., Liu, X., Watanabe, N., Selamoglu, Z., Ali, M., Li, X., & Li, J. (2019). Curcumol: From Plant Roots to Cancer Roots. *International Journal Of Biological Sciences*, *15*(8), 1600–1609. https://doi.org/10.7150/ijbs.34716
18. Wang, J., Jin, J., Chen, T., & Zhou, Q. (2022). Curcumol Synergizes with Cisplatin in Osteosarcoma by Inhibiting M2-like Polarization of Tumor-Associated Macrophages. *Molecules*, *27*(14). https://doi.org/10.3390/molecules27144345
19. Yang, L., Xiong, H., Li, X., Li, Y., Zhou, H., Lin, X., Chan, T. F., Li, R., Lai, K. P., & Chen, X. (2022). Network Pharmacology and Comparative Transcriptome Reveals Biotargets and Mechanisms of Curcumol Treating Lung Adenocarcinoma Patients With COVID-19, Front. *Nutr Volume*, *9*, 870370. https://doi.org/10.3389/fnut.2022.870370
20. Meng, X. W., Wei, Y. Y., Nong, B. L., Zhao, H. J., & Zhang, X. X. (2022). Design, synthesis, and anticancer activity evaluation of curcumol derivatives. *Journal Of Asian Natural Products Research*, *24*(6), 556–568. https://doi.org/10.1080/10286020.2021.1947255
21. Wang, D., Luo, F., He, F., Lu, F., Tao, X., Song, K., Zhao, J., & Chen, L. (2021). Preparation and anti-tumor activity of PEG-PCL polymersomes loaded with curcumol derivative in HepG2 cell line. *Journal Of Drug Delivery Science And Technology*, *66*, 102782. https://doi.org/10.1016/j.jddst.2021.102782
22. Jiang, Y., Yan, C., Li, M., Chen, S., Chen, Z., Yang, L., & Luo, K. (2024). Delivery of natural products via polysaccharide-based nanocarriers for cancer therapy: A review on recent advances and future challenges. *International Journal Of Biological Macromolecules*, *278*(Pt 4), 135072. https://doi.org/10.1016/j.ijbiomac.2024.135072
23. Parks, S. K., Mueller-Klieser, W., & Pouysségur, J. (2020). Lactate and Acidity in the Cancer Microenvironment. *Annu Rev Cancer Biol*, *4*, 141–158. https://doi.org/10.1146/annurev-cancerbio-030419-033556
24. Boedtkjer, E., & Pedersen, S. F. (2020). The Acidic Tumor Microenvironment as a Driver of Cancer. *Annual Review Of Physiology*, *82*, 103–126. https://doi.org/10.1146/annurev-physiol-021119-034627
25. Gharehbaba, A. M., Soltanmohammadi, F., Eskandani, M., & Adibkia, K. (2026). Emerging roles of mesoporous silica nanoparticles in personalized medicine: revolutionizing therapy and diagnosis — a comprehensive review. *Results Eng*, *30*, 110396. https://doi.org/10.1016/j.rineng.2026.110396
26. Zhou, S., Zhong, Q., Wang, Y., Hu, P., Zhong, W., Huang, C. B., Yu, Z. Q., Ding, C. D., Liu, H., & Fu, J. (2022). Chemically engineered mesoporous silica nanoparticles-based intelligent delivery systems for theranostic applications in multiple cancerous/non-cancerous diseases. *Coordination Chemistry Reviews*, *452*, 214309. https://doi.org/10.1016/j.ccr.2021.214309
27. Kesse, S., Boakye-Yiadom, K. O., Ochete, B. O., Opoku-Damoah, Y., Akhtar, F., Filli, M. S., Asim Farooq, M., Aquib, M., Maviah Mily, B. J., Murtaza, G., & Wang, B. (2019). Mesoporous Silica Nanomaterials: Versatile Nanocarriers for Cancer Theranostics and Drug and Gene Delivery, Pharmaceutics 11(2) 77. https://doi.org/10.3390/pharmaceutics11020077

28. Fan, H., & Guo, Z. (2023). Tumor microenvironment-responsive manganese-based nanomaterials for cancer treatment. *Coordination Chemistry Reviews*, *480*, 215027. https://doi.org/10.1016/j.ccr.2023.215027
29. Li, X., Zhang, X., Zhao, Y., & Sun, L. (2020). Fabrication of biodegradable Mn-doped mesoporous silica nanoparticles for pH/redox dual response drug delivery. *Journal Of Inorganic Biochemistry*, *202*, 110887. https://doi.org/10.1016/j.jinorgbio.2019.110887
30. Yu, L., Chen, Y., Wu, M., Cai, X., Yao, H., Zhang, L., Chen, H., & Shi, J. (2016). Manganese Extraction Strategy Enables Tumor-Sensitive Biodegradability and Theranostics of Nanoparticles. *Journal Of The American Chemical Society*, *138*(31), 9881–9894. https://doi.org/10.1021/jacs.6b04299
31. Huang, X., Li, G., Li, H., Zhong, W., Jiang, G., Cai, J., Xiong, Q., Wu, C., Su, K., Huang, R., Xu, S., Liu, Z., Wang, M., & Wang, H. (2024). Glycyrrhetinic Acid as a Hepatocyte Targeting Ligand-Functionalized Platinum(IV) Complexes for Hepatocellular Carcinoma Therapy and Overcoming Multidrug Resistance. *Journal Of Medicinal Chemistry*, *67*(10), 8020–8042. https://doi.org/10.1021/acs.jmedchem.4c00144
32. Zhang, D., Liu, Y., Wang, M., Lyu, H., & Sun, Y. (2025). The antitumor mechanism of glycyrrhetinic acid and its applications in cancer treatment. *Medical Oncology*, *42*(8), 331. https://doi.org/10.1007/s12032-025-02904-0
33. Wu, S., Wang, W., Dou, J., & Gong, L. (2021). Research progress on the protective effects of licorice-derived 18β-glycyrrhetinic acid against liver injury. *Acta Pharmacologica Sinica*, *42*(1), 18–26. https://doi.org/10.1038/s41401-020-0383-9
34. Cai, Y., Xu, Y., Chan, H. F., Fang, X., He, C., & Chen, M. (2016). Glycyrrhetinic Acid Mediated Drug Delivery Carriers for Hepatocellular Carcinoma Therapy. *Molecular Pharmaceutics*, *13*(3), 699–709. https://doi.org/10.1021/acs.molpharmaceut.5b00677
35. Speciale, A., Muscarà, C., Molonia, M. S., Cristani, M., Cimino, F., & Saija, A. (2022). Recent Advances in Glycyrrhetinic Acid-Functionalized Biomaterials for Liver Cancer-Targeting Therapy. *Molecules*, *27*(6), 1775. https://doi.org/10.3390/molecules27061775
36. Liu, Z., Xie, H., & Wang, T. (2023). Erythrocyte–Cancer Hybrid Membrane-Camouflaged Prussian Blue Nanoparticles with Enhanced Photothermal Therapy in Tumors. *ACS Omega*, *8*(25), 23056–23066. https://doi.org/10.1021/acsomega.3c02370
37. Yang, B., Xiao, B., & Sun, T. (2013). Antitumor and immunomodulatory activity of Astragalus membranaceus polysaccharides in H22 tumor-bearing mice. *International Journal Of Biological Macromolecules*, *62*, 287–290. https://doi.org/10.1016/j.ijbiomac.2013.09.016
38. Sha, Z., Yang, S., Fu, L., Geng, M., Gu, J., Liu, X., Li, S., Zhou, X., & He, C. (2021). Manganese-doped gold core mesoporous silica particles as a nanoplatform for dual-modality imaging and chemo-chemodynamic combination osteosarcoma therapy. *Nanoscale*, *13*(9), 5077–5093. https://doi.org/10.1039/d0nr09220g
39. Huang, R., Shen, Y. W., Guan, Y. Y., Jiang, Y. X., Wu, Y., Rahman, K., Zhang, L. J., Liu, H. J., & Luan, X. (2020). Mesoporous silica nanoparticles: facile surface functionalization and versatile biomedical

applications in oncology. *Acta Biomaterialia*, *116*, 1–15. https://doi.org/10.1016/j.actbio.2020.09.009

40. Chen, H. C., Shi, Q. X., Dhawan, U., Wu, K. C. W., & Chung, R. J. (2026). Surface modified mesoporous silica nanoparticles for sustained drug release and long-term therapeutic effects. *Journal Of The Australian Ceramic Society*. https://doi.org/10.1007/s41779-026-01378-1
41. Qin, G., Xie, W., Luo, X., Zou, G., Mo, Q., & Zhong, W. (2024). Manganese-doped stellate mesoporous silica nanoparticles: A bifunctional nanoplatform for enhanced chemodynamic therapy and tumor imaging. *Microporous And Mesoporous Materials*, *370*, 113012. https://doi.org/10.1016/j.micromeso.2024.113012
42. Wu, X., Wen, X., Lin, X., Wang, X., Wan, Y., Gao, R., Zhang, Y., & Han, C. (2024). pH/glutathione-responsive theranostic nanoprobes for chemoimmunotherapy and magnetic resonance imaging of ovarian cancer cells. *Colloids And Surfaces. B, Biointerfaces*, *241*, 114053. https://doi.org/10.1016/j.colsurfb.2024.114053
43. Luo, J., Panzarasa, G., Osypova, A., Sorin, F., Spano, F., Rossi, R. M., Sadeghpour, A., & Boesel, L. F. (2019). Polyphenols as Morphogenetic Agents for the Controlled Synthesis of Mesoporous Silica Nanoparticles. *Chemistry Of Materials*, *31*(9), 3192–3200. https://doi.org/10.1021/acs.chemmater.8b05249
44. Bavnhøj, C. G., Knopp, M. M., & Löbmann, K. (2024). Effect of Drug Loading in Mesoporous Silica on Amorphous Stability and Performance. *Pharmaceutics*, *16*(2), 163. https://doi.org/10.3390/pharmaceutics16020163
45. Hao, C., Shao, Y., Tian, J., Song, J., & Song, F. (2024). Dual-Responsive hollow mesoporous organosilicon nanocarriers for photodynamic therapy. *Journal Of Colloid And Interface Science*, *659*, 582–593. https://doi.org/10.1016/j.jcis.2024.01.034
46. Tang, H., Li, C., Zhang, Y., Zheng, H., Cheng, Y., Zhu, J., Chen, X., Zhu, Z., Piao, J. G., & Li, F. (2020). Targeted Manganese doped silica nano GSH-cleaner for treatment of Liver Cancer by destroying the intracellular redox homeostasis. *Theranostics*, *10*(21), 9865–9887. https://doi.org/10.7150/thno.46771
47. Ling, J., Jiang, Y., Yan, S., Dang, H., Yue, H., Liu, K., Kuang, L., Liu, X., & Tang, H. (2022). A novel pH- and glutathione-responsive drug delivery system based on in situ growth of MOF199 on mesoporous organic silica nanoparticles targeting the hepatocellular carcinoma niche. *Cancer Nanotechnology*, *13*(1), 32. https://doi.org/10.1186/s12645-022-00139-6
48. Zhang, J. Y., Su, Y. H., Wang, X., Yao, X., & Du, J. Z. (2024). Recent Progress on Nanomedicine-Mediated Repolarization of Tumor-Associated Macrophages for Cancer Immunotherapy, WIREs Nanomed. Nanobiotechnol. 16(5) e2001. https://doi.org/10.1002/wnan.2001
49. Li, C., Wang, L., Li, Z., Li, Z., Zhang, K., Cao, L., Wang, Z., Shen, C., & Chen, L. (2024). Repolarizing Tumor-Associated Macrophages and inducing immunogenic cell Death: A targeted liposomal strategy to boost cancer immunotherapy. *International Journal Of Pharmaceutics*, *651*, 123729. https://doi.org/10.1016/j.ijpharm.2023.123729

50. Lv, Y., Li, J., Chen, H., Bai, Y., & Zhang, L. (2017). Glycyrrhetinic acid-functionalized mesoporous silica nanoparticles as hepatocellular carcinoma-targeted drug carrier. *Int J Nanomedicine*, *12*, 4361–4370. https://doi.org/10.2147/ijn.S135626

51. Xi, X., Wang, X., Xi, Z., Fan, C., Jiang, Y., Li, Z., & Xu, L. (2025). Facile GSH responsive glycyrrhetinic acid conjunction for liver targeting therapy. *Chinese Chemical Letters*, *36*(10), 110773. https://doi.org/10.1016/j.cclet.2024.110773

52. Sun, L., Sogo, Y., Wang, X., & Ito, A. (2021). Biosafety of mesoporous silica nanoparticles: a combined experimental and literature study. *J Mater Sci Mater Med*, *32*(9), 102. https://doi.org/10.1007/s10856-021-06582-y

Scheme 1

Scheme 1 is available in the Supplementary Files section.

Figures

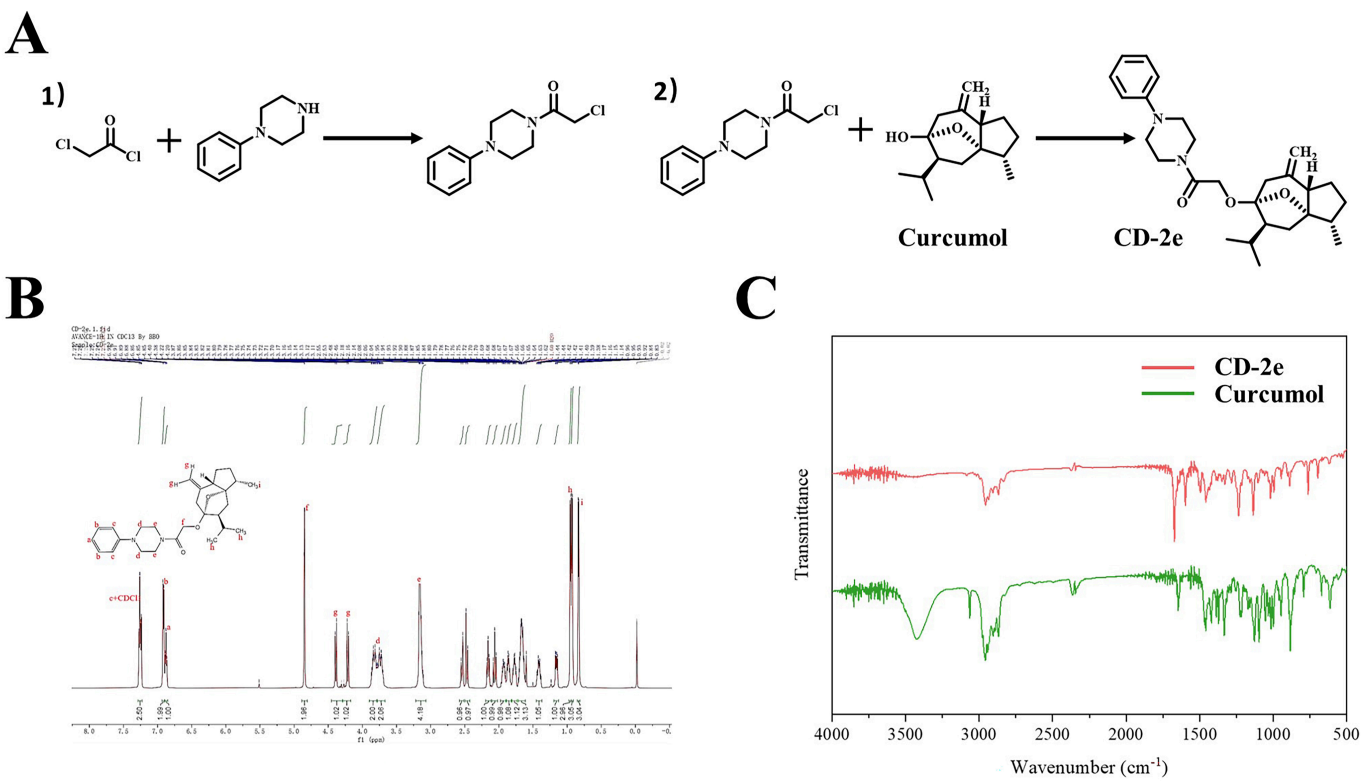


Figure 1

(A) Synthesis of CD2e. (B) ^{1}H NMR spectra of CD2e. (C) FT-IR spectra of curcumol and CD2e.

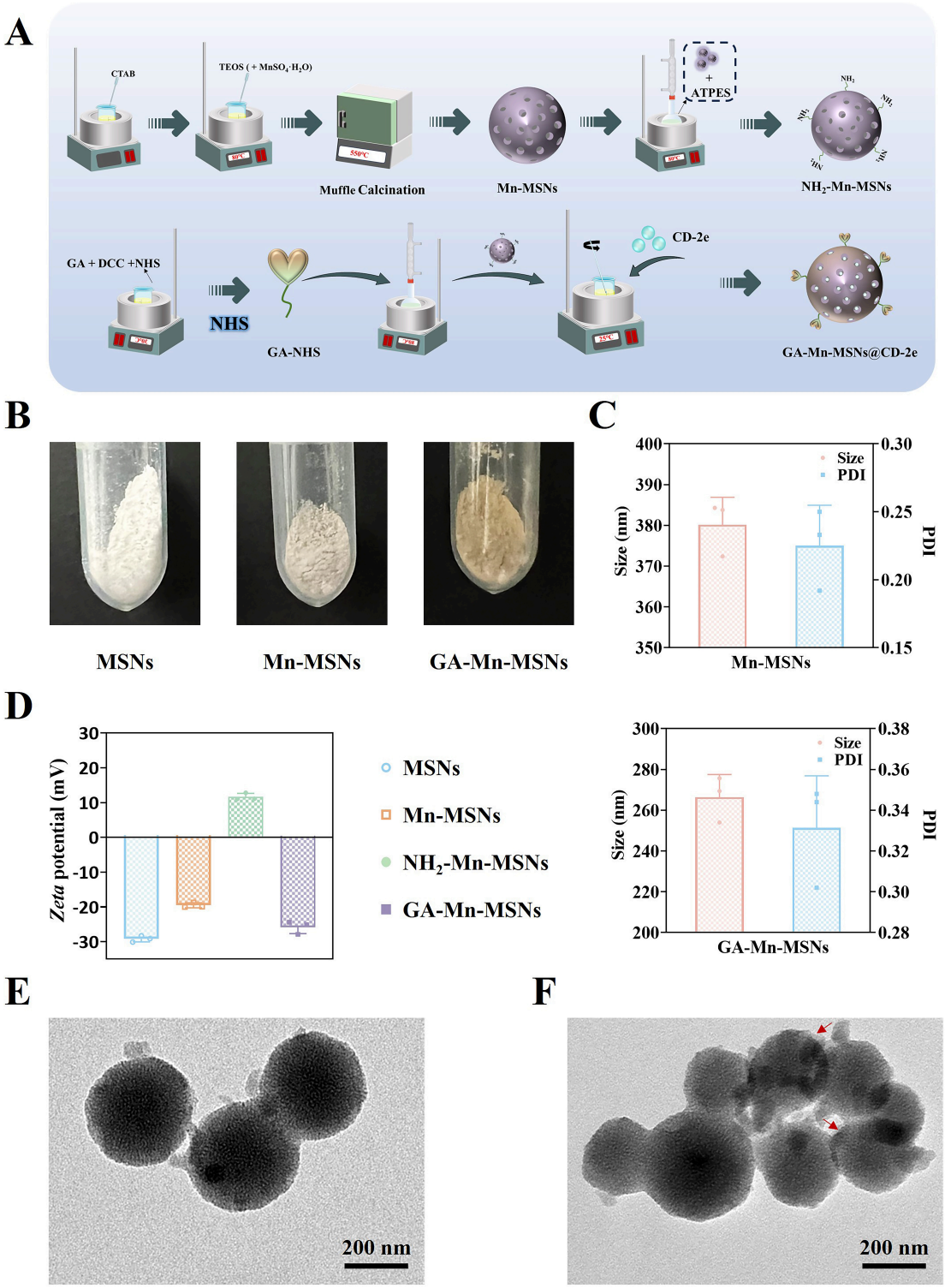


Figure 2

(A) Schematic illustration of the synthesis of GA-Mn-MSNs@CD-2e. (B) Photographs of MSNs, Mn-MSNs, and GA-Mn-MSNs. (C) Particle size and polydispersity index (PDI) of Mn-MSNs and GA-Mn-MSNs. (D) Zeta potentials of MSNs, Mn-MSNs, NH_2-Mn-MSNs, and GA-Mn-MSNs. (E) TEM image of Mn-MSNs. Scale bar = 50 nm. (F) TEM image of GA-Mn-MSNs. Scale bar = 50 nm. Data are presented as mean ± SD, n = 3.

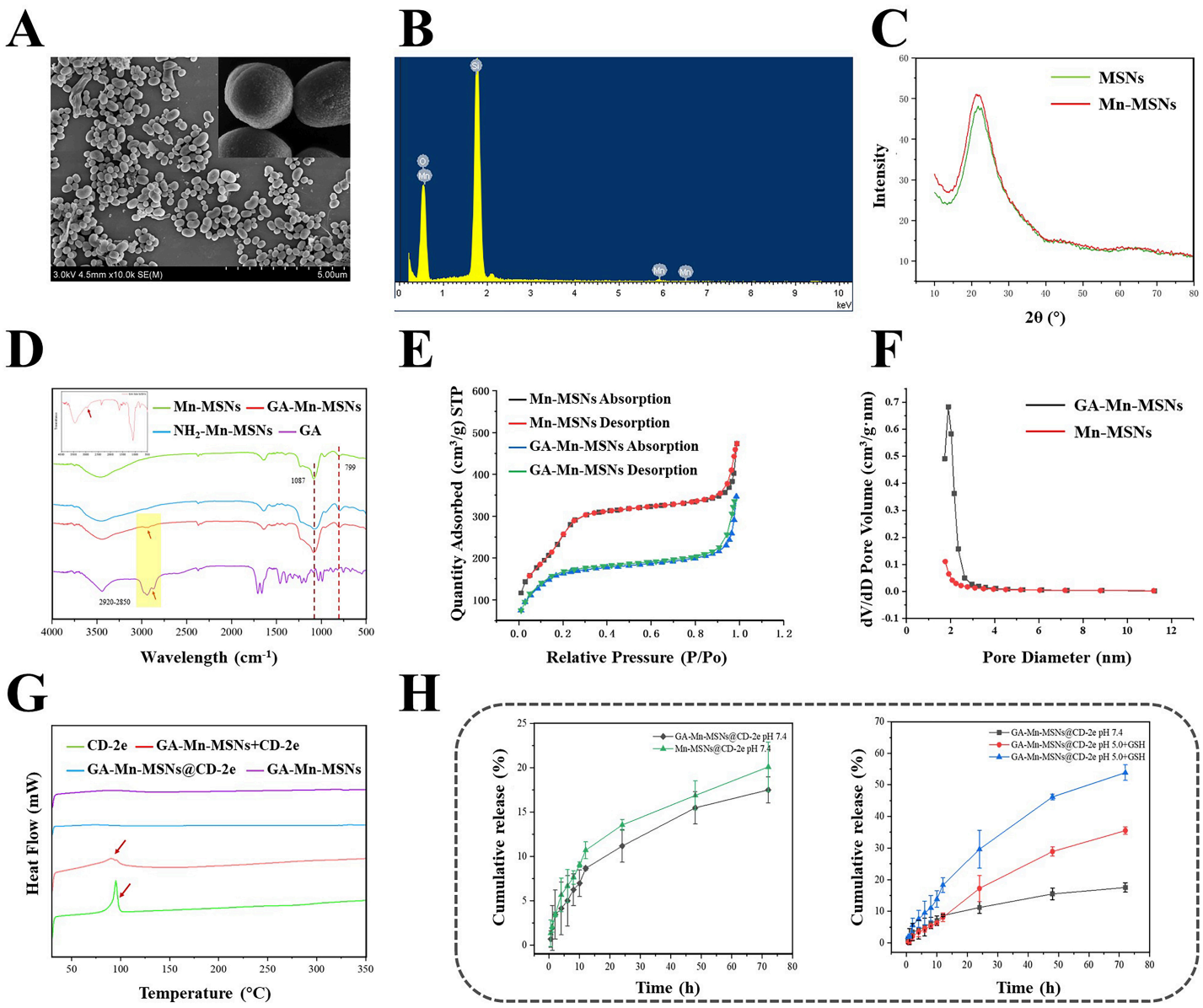


Figure 3

(A) SEM image of Mn-MSNs. (B) EDS spectrum of Mn-MSNs. (C) X-ray diffraction patterns of MSNs and Mn-MSNs. (D) FT-IR spectra of Mn-MSNs, NH_2-Mn-MSNs, GA-Mn-MSNs, and GA. (E) N_2 adsorption-desorption isotherms of Mn-MSNs and GA-Mn-MSNs. (F) Pore size distribution curves of Mn-MSNs and GA-Mn-MSNs. (G) DSC curves of CD-2e, GA-Mn-MSNs, GA-Mn-MSNs@CD-2e, and the physical mixture of GA-Mn-MSNs and CD-2e. (H) *In vitro* cumulative drug release profiles of Mn-MSNs@CD-2e and GA-Mn-MSNs@CD-2e under different pH conditions. Data are presented as mean ± SD, n = 3.

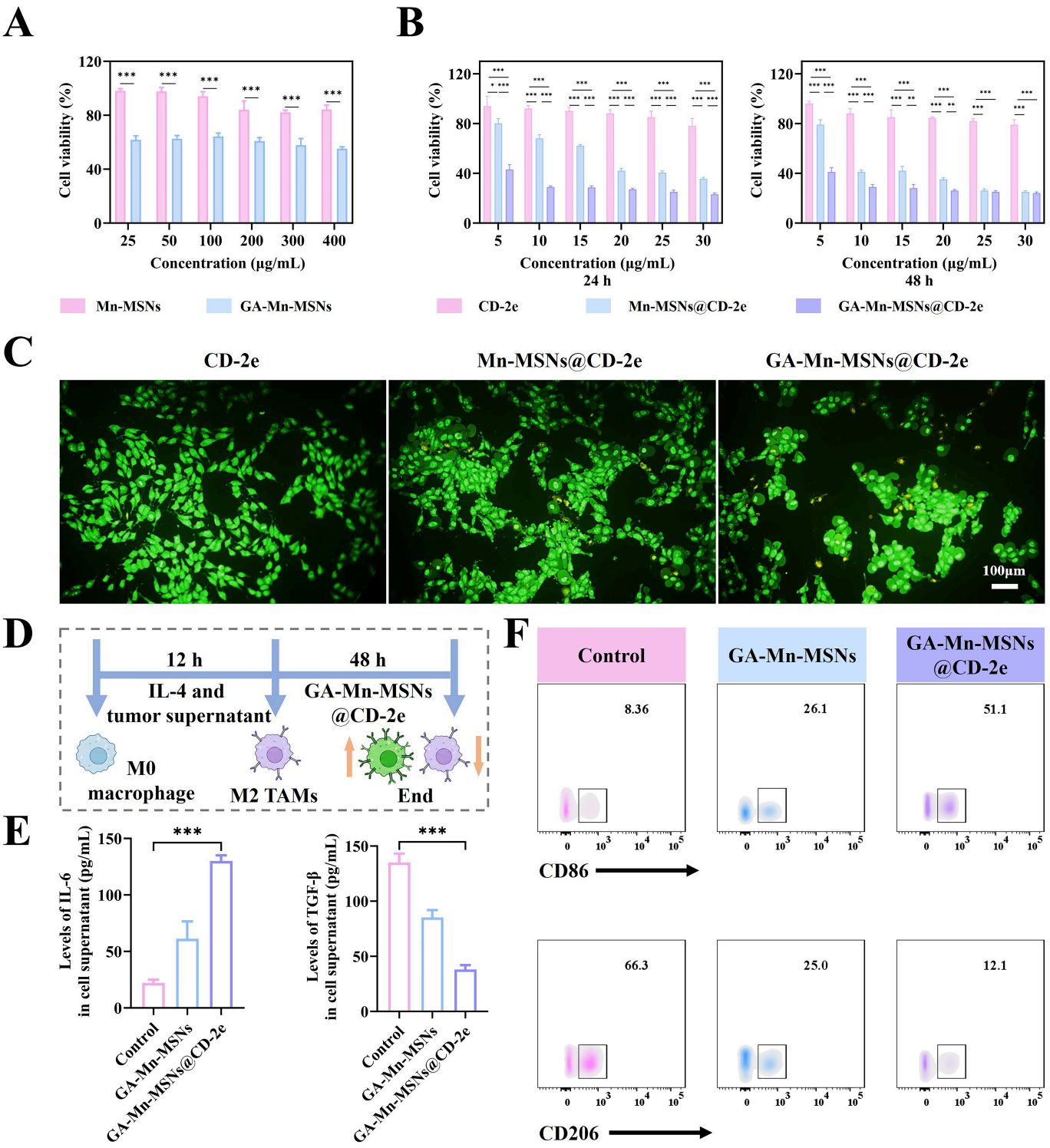


Figure 4

(A) *In vitro* cytotoxicity of MnMSNs and GAMnMSNs to HepG2 cells. (B) *In vitro* cytotoxicity of CD2e, Mn-MSNs@CD2e, and GAMnMSNs@CD2e to HepG2 cells. (C) CD2e, MnMSNs@CD2e, and GAMn-MSNs@CD2e induced apoptosis in HepG2 cells. (D) Schematic illustration of the experimental procedure for macrophage polarization. (E) ELISA analysis of IL-6 and TGF-β levels in cell culture supernatants after different treatments. IL-6 was used as an indicator of the M1-like pro-inflammatory

phenotype, whereas TGF-β was used as an indicator of the M2-like immunosuppressive phenotype. (F) Flow cytometric analysis of changes in CD86 and CD206 expression in TAMs following different treatments. Data are presented as mean ± SD, n = 3. $^{*}P < 0.05$, $^{**}P < 0.01$, $^{***}P < 0.001$.

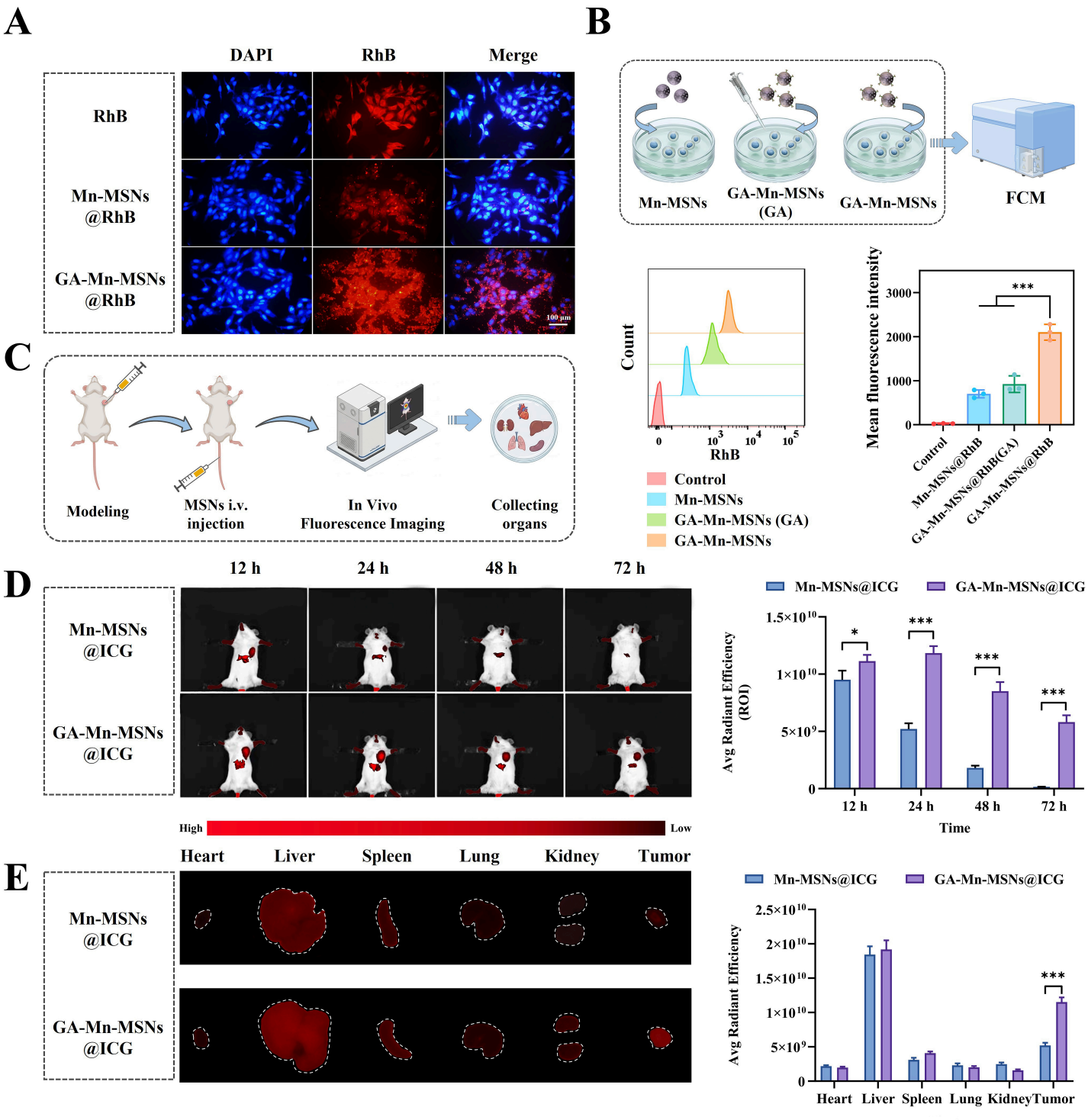


Figure 5

(A) FIM images showing the cellular uptake of free RhB, Mn-MSNs@RhB, and GA-Mn-MSNs@RhB in HepG2 cells. Scale bar = 100 μm (B) FCM analysis of different formulations in HepG2 cells. (C) Schematic illustration of the *in vivo* fluorescence imaging procedure in tumor-bearing mice. (D) *In vivo* fluorescence imaging and quantitative ROI analysis of tumor-bearing mice after intravenous injection of Mn-MSNs@ICG and GA-Mn-MSNs@ICG at different time points. (E) *Ex vivo* fluorescence imaging of major organs and tumors collected 72 h after injection, and corresponding quantitative analysis. Data are expressed as mean ± SD, n = 3. $^{**}P < 0.01$, $^{***}P < 0.001$.

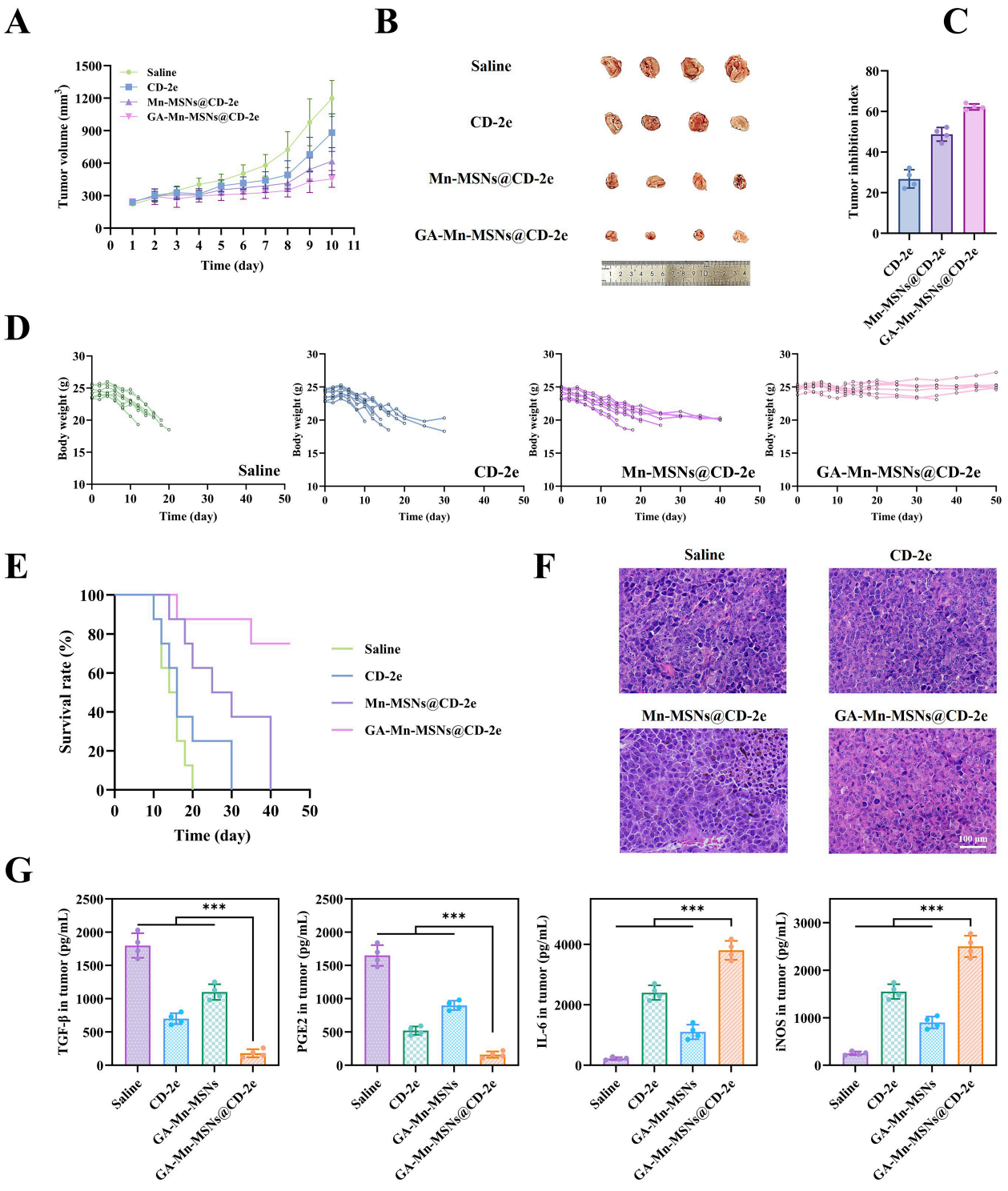


Figure 6

(A) Dynamic changes in tumor volume in different treatment groups. (B) Representative images of excised tumors from each group on Day 10. (C) Tumor inhibition rate index of each group on Day 10. (D) Changes in body weight of tumor-bearing mice in different treatment groups throughout the observation period. (E) Survival curves of tumor-bearing mice in different treatment groups. (F) H&E staining results of tumor tissues from different treatment groups on Day 10. Scale bar = 100 μm. (G) Secretion levels of TGF-β, PGE2, IL-6, iNOS in tumor tissues measured by ELISA. Data are expressed as mean ± SD, $^{***}P < 0.001$.

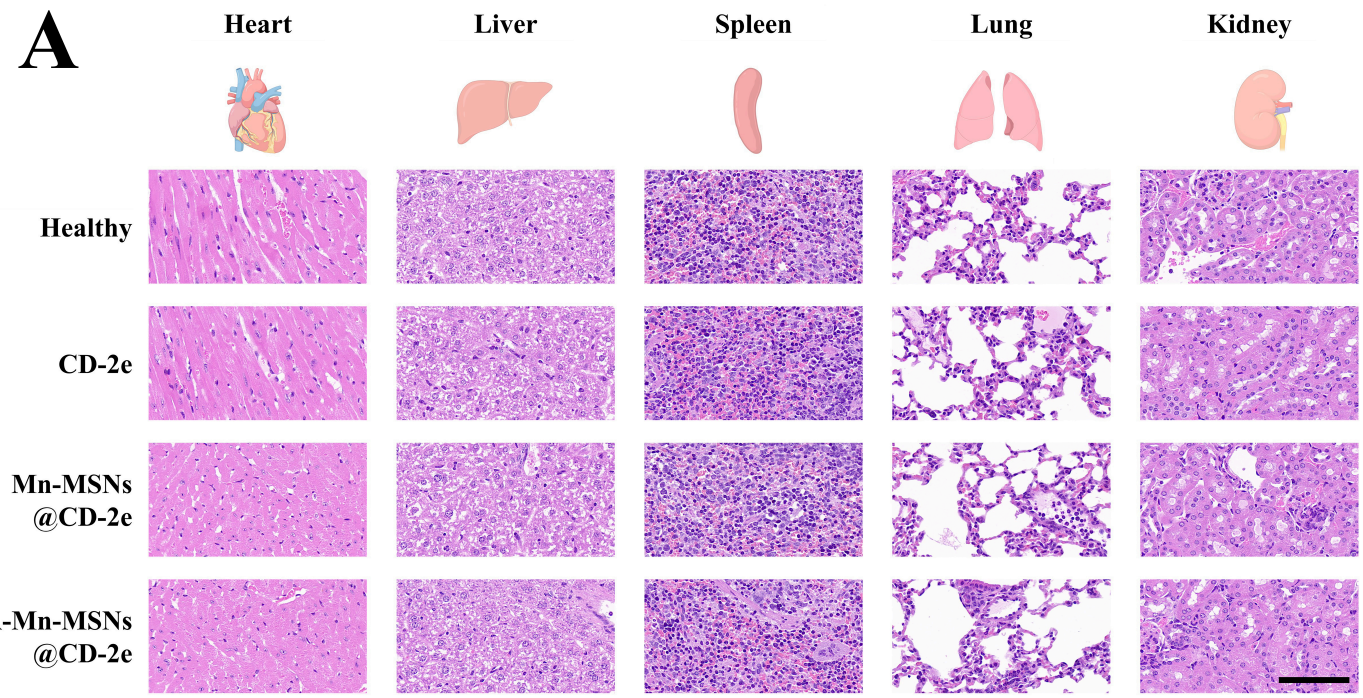


Figure 7

(A) H&E-stained sections of the major organs after treatment. Scale bar = 50 μm.

Supplementary Files

This is a list of supplementary files associated with this preprint. Click to download.

- Supplementarymaterials.docx
- Scheme1.jpg